



1 **Enhancing SO₃ Hydrolysis and Nucleation: The Role of** 2 **Formic Sulfuric Anhydride**

3 **Rui Wang^a, Rongrong Li^a, Shasha Chen^a, Ruxue Mu^a, Changming Zhang^b,**
4 **Xiaohui Ma^{c,*}, Majid Khan^d, Tianlei Zhang^{a,*}**

5 ^a *Shaanxi Key Laboratory of Catalysis, School of Chemical & Environment Science, Shaanxi*
6 *University of Technology, Hanzhong, Shaanxi 723001, P. R. China*

7 ^b *Shaanxi Key Laboratory of Catalysis, School of Mechanical Engineering, Shaanxi University of*
8 *Technology, Hanzhong, Shaanxi 723001, P. R. China*

9 ^c *School of Environmental Engineering, Henan University of Technology, Zhengzhou, Henan*
10 *450001, China*

11 ^d *College of Chemistry, Fuzhou University, 350116, Fuzhou, China*

12

13 **Abstract**

14 Although the nucleation route driven by sulfuric acid (H₂SO₄) and ammonia (NH₃) primarily
15 dominates new particle formation (NPF) in the atmosphere, exploring the role of other trace species
16 on H₂SO₄-NH₃ system is crucial for a more comprehensive insight into NPF processes. Formic
17 sulfuric anhydride (FSA) has been observed in atmospheric environment and is found in abundance
18 in atmospheric fine particles. Nevertheless, its effect on SO₃ hydrolysis and NPF remain poorly
19 understood. Here, we studied the enhancing effect of FSA on gaseous and interfacial SO₃ hydrolysis
20 as well as its impact on H₂SO₄-NH₃-driven NPF occurring through quantum chemical calculations,
21 atmospheric clusters dynamics code (ACDC) kinetics combined with Born-Oppenheimer molecular
22 dynamics (BOMD). Gaseous-phase findings indicate that FSA-catalyzed SO₃ hydrolysis is nearly
23 barrierless. At an [FSA] = 10⁷ molecules·cm⁻³, this reaction competes effectively with SO₃
24 hydrolysis in the presence of HNO₃ (10⁹ molecules·cm⁻³), HCOOH (10⁸ molecules·cm⁻³) and H₂SO₄
25 (10⁶ molecules·cm⁻³) in the range of 280.0-320.0 K. At the gas-liquid nanodroplet interface, BOMD
26 simulations reveal that FSA-mediated SO₃ hydrolysis follows a stepwise mechanism, completing
27 within a few picoseconds. Notably, FSA enhances the formation rate of H₂SO₄-NH₃ clusters by over
28 10⁷ times in regions with relatively high [FSA] at elevated temperatures. Additionally, interfacial
29 FSA⁻ ion has the ability to appeal precursor species for particle formation from the gaseous phase
30 to the water nanodroplet interface, thereby facilitating particle growth. These results present new
31 comprehensions into both the pathways of H₂SO₄ formation and aerosol particle growth in polluted
32 boundary layer.

33 **Keywords:** gas phase, atmospheric behavior, new particle formation, air pollution

* Corresponding authors. Tel: +86-0916-2641083, Fax: +86-0916-2641083.

e-mail: ztianlei88@163.com (T. L. Zhang) and mxhsdu@163.com (X. H. Ma)



34 1. Introduction

35 Sulfuric acid (H_2SO_4) is an important atmospheric pollutant closely associated with new
36 particle formation (NPF) events and is recognized as a vital precursor in the process of converting
37 gases into particles. It facilitates the formation of sulfate aerosols and acid rain in diverse
38 environments, influencing cloud formation, precipitation and the Earth's radiation balance,
39 ultimately contributing to climate change (Yao et al., 2018; Venkataraman et al., 2001; Kumar et
40 al., 2024). Experimental (Couling et al., 2003; Reiner and Arnold, 1993; Bondybey and English,
41 1985) and theoretical studies (Feng and Wang, 2023; Kumar et al., 2024; Zhang et al., 2025) have
42 shown that atmospheric gaseous H_2SO_4 primarily forms via SO_3 hydrolysis (Sarkar et al., 2019; Tao
43 et al., 2018; Carmona-García et al., 2021). However, the likelihood of direct SO_3 hydrolysis in the
44 atmosphere is low due to the high activation energy associated with the process (Chen and Plummer,
45 1985). Introducing a second water molecule has been shown to significantly lower the activation
46 energy, making SO_3 hydrolysis more efficient (Morokuma and Muguruma, 1994). Further research
47 indicates that, besides water molecules, other species such as formic acid (Kangas et al., 2020),
48 oxalic acid (Yang et al., 2021), nitric acid (Long et al., 2022), H_2SO_4 (Wang et al., 2024) and
49 ammonia (Sarkar et al., 2019) exhibit even greater catalytic efficiency in promoting SO_3 hydrolysis
50 for H_2SO_4 formation. These findings provide valuable theoretical insights for understanding H_2SO_4
51 sources, particularly in regions where pollutant concentrations are notably elevated. Nevertheless,
52 further investigation is necessary to fully understand the SO_3 hydrolysis mechanism in areas with
53 high levels of specific pollutants, to better assess its behavior and effects under different atmospheric
54 conditions.

55 Carboxylic sulfuric anhydrides (CSAs) are a recently identified class of atmospheric
56 organosulfides, formed by the cycloaddition of SO_3 with organic carboxylic acids present (Fleig et
57 al., 2012). These CSAs exhibit strong acidity and can act as proton transfer bridges, potentially
58 influencing SO_3 hydrolysis and promoting the formation of H_2SO_4 in regions with high CSA
59 concentrations. Research indicates that the gaseous CSA concentration can reach 10^7 molecules·cm⁻³
60 (Smith et al., 2020), creating conditions that may impact SO_3 hydrolysis. As the simplest CSA,
61 formic sulfuric anhydride (FSA) has been characterized using microwave spectroscopic (Mackenzie
62 et al., 2015). FSA is more acidic than formic acid and may facilitate proton transfer in the gaseous



63 hydrolysis of SO_3 . However, its role in this process has not yet been explored. Besides, it has been
64 reported that the interfacial environment both initiates the organization and clustering of hydrophilic
65 groups and acts as an effective medium for various atmospheric reactions (Ma et al., 2020; Zhong
66 et al., 2019; Tan et al., 2022; Wan et al., 2023). Notably, proton transfer routes induced by interfacial
67 water molecules accelerate numerous atmospheric reactions taking place on aerosols and droplets
68 surfaces. These reactions typically proceed at accelerated rates and can differ from similar processes
69 in the gas phase or bulk water (Tang et al., 2024; Fang et al., 2024; Martins-Costa and Ruiz-López,
70 2024). Thus, it is essential to investigate whether FSA accelerates SO_3 hydrolysis at the gas-liquid
71 nanodroplet interface, as this could offer valuable insights into atmospheric chemistry and the
72 mechanisms driving particle formation

73 Additionally, new species generated from gas-phase reactions of SO_3 with trace substances (Li
74 et al., 2018; Liu et al., 2019) can also significantly influence the NPF process. For example, Li et al.
75 (Li et al., 2018) revealed that $\text{NH}_2\text{SO}_3\text{H}$, formed from the reaction of SO_3 with NH_3 , not only
76 contributes directly to $\text{H}_2\text{SO}_4\text{-(CH}_3)_2\text{NH}$ cluster formation but also enhances the maximum rate of
77 NPF from H_2SO_4 and $(\text{CH}_3)_2\text{NH}$ by approximately twofold in heavily polluted areas with high
78 concentrations of basic substances. Similarly, Liu et al. (Liu et al., 2019) predicted that methyl
79 hydrogen sulfate (MHS), formed from the reaction of SO_3 with methanol, significantly impacts
80 $\text{H}_2\text{SO}_4\text{-(CH}_3)_2\text{NH}$ nucleation, particularly in dry regions with high alcohol concentrations. FSA,
81 produced from the reaction of SO_3 with HCOOH , contains the $-\text{OSO}_3\text{H}$ functional group and
82 exhibits a binding capability comparable to that of H_2SO_4 with nucleation precursors like NH_3 . The
83 potential role of FSA in enhancing $\text{H}_2\text{SO}_4\text{-NH}_3$ nucleation in the atmosphere requires further
84 investigation to fully understand its contribution to NPF processes.

85 This work examined the catalytic effect of FSA on SO_3 hydrolysis and $\text{H}_2\text{SO}_4\text{-NH}_3$ nucleation
86 particle formation. Specifically, the catalytic effects of FSA on gaseous SO_3 hydrolysis were firstly
87 explored. Following this, the differences between the gaseous and interfacial reactions of FSA-
88 catalyzed SO_3 hydrolysis were evaluated using BOMD simulations. Subsequently, a qualitative
89 evaluation of FSA's nucleation capability was conducted through molecular dynamics (MD)
90 simulations. Finally, the atmospheric implications of FSA on particle formation were analyzed. This
91 study not only deepens our understanding of the impact of FSA on SO_3 hydrolysis but also provides
92 new molecular-level mechanisms for the contribution to $\text{H}_2\text{SO}_4\text{-NH}_3$ particle formation.



93 2. Computational Methods

94 **2.1 Quantum Chemical Details.** To investigate the impact of formic sulfuric anhydride
95 (FSA) on gaseous SO₃ hydrolysis, the M06-2X/6-311++G(2df,2pd) computational method, as
96 implemented in Gaussian 09 software (Frisch, 2009), was employed to analyze the geometric
97 structures and vibrational frequencies of the relevant species. We also carried out the
98 calculation of intrinsic reaction coordinate to conduct the connections between the transition
99 states and their corresponding pre-reactive and post-reactive complexes. To enhance the
100 reliability of the relative Gibbs free energies, single-point energies at the CCSD(T)-F12/cc-
101 pVDZ-F12 level were calculated using the ORCA software (Neese, 2012).

102 The most stable structure of the (FSA)_x(SA)_y(A)_z ($z \leq x + y \leq 3$) clusters were obtained by
103 the following three steps. Initially, the ABCcluster program (Zhang and Dolg, 2015) was utilized to
104 randomly produce $n \times 1000$ initial isomers (where $n = 2$ to 4) which were subsequently evaluated
105 using the PM6 method via MOPAC 2016 (Partanen et al., 2016). Next, up to $n \times 100$ lowest-energy
106 isomers were chosen and further refined using the method of M06-2X/6-31+G(*d,p*). Lastly, the top
107 $n \times 10$ isomers were re-optimized at the M06-2X/6-311++G(2df,2pd) method level to ascertain their
108 isomers with the lowest energy. The optimized structures and their Gibbs free energies are detailed
109 in Fig. S10 and Table S6, respectively.

110 **2.2 Rate Coefficient Computations.** Rate coefficients for FSA-assisted SO₃ hydrolysis were
111 calculated via two steps as follows. First, the VRC-VTST methodology (Zhang et al., 2023; Zhang
112 et al., 2024) was applied using the Polyrate program (Meana-Pañeda et al., 2024) to calculate the
113 rate coefficients under high-pressure conditions. Next, the Master Equation Solver for Multi-Energy
114 Well Reactions (Glowacki et al., 2012) was engaged in computing the rate coefficients for FSA-
115 assisted SO₃ hydrolysis across a temperature range of 280.0 to 320.0 K. To estimate the rate
116 coefficients for the barrier less formation of pre-reactive complexes from the separated reactants,
117 we applied the Inverse Laplace Transform (ILT) method (Kumar et al., 2021). In parallel, RRKM
118 theory (Bao et al., 2016) was utilized to estimate the rate coefficients for the transition from the pre-
119 reactive complex to the post-reactive complex through a transition stat. Details of the ILT methods
120 and RRKM theory are provided in Part 1 and Part 2 in the Supplement, respectively.

121 **2.3 BOMD Simulations.** BOMD simulations were conducted with the CP2K program



122 (Hutter et al., 2014). The BLYP functional was applied to address exchange and correlation
123 interactions (Becke, 1988; Lee et al., 1988). Grimme's dispersion-corrected method (Grimme
124 et al., 2010) was employed to account for the dispersion interactions and effectively handle
125 weak dispersion effects. The Goedecker-Teter-Hutter conservation pseudopotentials
126 (Goedecker et al., 1996) were done by using Gaussian DZVP basis set (Phillips et al., 2005)
127 and an auxiliary plane wave basis, ensuring accurate treatment of both valence and core
128 electrons. The plane wave basis set was established with a 280 Ry energy cutoff, while the Gaussian
129 basis set cutoff was set at 40 Ry. A supercell side length of 15 Å was used in gas phase simulations
130 to eliminate periodic boundary conditions with step of 0.5 fs. For interfacial reactions, a water
131 droplet containing 191 water molecules was initially pre-optimized through BOMD simulation for
132 approximately 5.0 ps at 300 K. Subsequently, SO₃ and FSA were positioned at the gas-liquid
133 nanodroplet interface to perform the simulations over 10 ps. A supercell side length of 35 Å was
134 set for gas-liquid nanodroplet interface simulations to prevent periodic interactions between
135 neighbouring water droplets, using a step of 1.0 fs. In all simulations under the NVT ensemble, a
136 stable temperature of 300 K was maintained using the Nose-Hoover thermostat.

137 **2.4 Molecular Dynamics Simulation of Nucleation.** Complete nucleation pathway was
138 simulated using the GROMACS 2024.3 software (Abraham et al., 2024), employing the general
139 AMBER force field, a widely utilized approach for modelling molecular dynamics (Li et al.,
140 2024b; Cheng et al., 2025; Zhao et al., 2019). The electrostatic potential was computed at M06-
141 2X/6-311++G(2df,2pd) level and the restrained electrostatic potential charges were determined
142 using Multiwfn 3.8 (Lu and Chen, 2012). The AMBER parameter and coordinate files were
143 constructed using Sobtop (Lu, 2023) and Packmol (Martínez et al., 2009), respectively. The
144 simulation was performed within a cubic simulation box, each side measuring 200 Å in length.
145 Following energy minimization, the system was further simulated under the NVT and NPT
146 ensembles at 298 K for durations of 100 ps and 40 ns, respectively. The Berendsen pressure coupling
147 method (Berendsen et al., 1984) and the velocity rescaling thermostat (Bussi et al., 2007) were used
148 to regulate pressure and temperature, respectively. The system applied periodic boundary conditions
149 to mimic an infinite environment, with a 1 fs time step. The electrostatic and van der Waals
150 interactions were set with a 1.4 nm cutoff distance, and the Particle-Mesh Ewald method (York et
151 al., 1993) was implemented for long-range electrostatics. Bond lengths were restricted by the



152 LINCS algorithm (Hess et al., 1997) to preserve structural integrity during the simulation.

153 **2.5 Atmospheric Cluster Dynamics Code (ACDC) Model.** The ACDC (McGrath et al.,
154 2012) was employed to investigate cluster formation rates and growth mechanisms for
155 (FSA)_x(SA)_y(A)_z clusters. The ACDC simulations were supplied with thermodynamic data,
156 which was derived from quantum chemical calculations performed by M06-2X/6-
157 311++G(2df,2pd). Accounting for all potential collision and evaporation processes, the
158 following formulation represents the birth-death equations:

$$159 \quad \frac{dc_i}{dt} = \frac{1}{2} \sum_{j < i} \beta_{j,(i-j)} C_j C_{(i-j)} + \sum_j \gamma_{(i+j) \rightarrow i} C_{i+j} - \sum_j \beta_{i,j} C_i C_j - \frac{1}{2} \sum_{j < i} \gamma_{i \rightarrow j} C_i + Q_i - S_i \quad (1)$$

160 In the above equation, c_i represents the concentration of i cluster, while $\beta_{i,j}$ stands for the
161 collision rate between i and j clusters. The term $\gamma_{(i+j) \rightarrow i}$ refers to the rate at which the larger $i+j$
162 cluster breaks down (or evaporates) into i and j clusters. Additionally, Q_i accounts for any possible
163 external source of i cluster. To consider the external losses of i cluster, a coagulation sink coefficient
164 of $2 \times 10^{-2} \text{ s}^{-1}$ was used, aligning with values typically found in polluted environments (Liu et al.,
165 2021b). In ACDC, boundary clusters must be sufficiently stable, which allows them to continue
166 growing. Therefore, the clusters of (FSA)₂·(SA)₂·(A)₃, (FSA)₁·(SA)₃·(A)₃, (SA)₄·(A)₃ and
167 (SA)₄·(A)₄ were selected as the boundary clusters in the SA-A-FSA system.

168 3. Results and discussion

169 3.1 The Hydrolysis of SO₃ Assisted by FSA

170 The SO₃ hydrolysis with HCOOSO₃H (FSA) can initially occur via the interaction between
171 SO₃ (or FSA) and H₂O to form SO₃···H₂O (or FSA···H₂O) dimer. Subsequently, the SO₃···H₂O
172 dimer collides with FSA, and the FSA···H₂O dimer interacts with SO₃. The predicted relative Gibbs
173 free energies of SO₃···H₂O was 0.8 kcal·mol⁻¹ at the CCSD(T)-F12/cc-pVDZ-F12/M06-2X/6-
174 311++G(2df,2pd) level, which is nearly previously reported values (-0.2 to 1.0 kcal·mol⁻¹) (Long et
175 al., 2013; Long et al., 2012; Lv et al., 2019; Bandyopadhyay et al., 2017). As compared with
176 FSA···H₂O, the binding free energy of SO₃···H₂O is less stable by 2.6 kcal·mol⁻¹, which leads to
177 the equilibrium coefficient of FSA···H₂O (2.63×10^{-18} - 2.49×10^{-19} molecules·cm⁻³) (Table S2)
178 being at least 10 times larger than that of SO₃···H₂O (2.45×10^{-20} - 5.10×10^{-21} molecules·cm⁻³ within
179 280.0-320.0 K). Under the available concentrations ([FSA] = 1.0×10^7 , [SO₃] = 1.0×10^3
180 molecules·cm⁻³) (Liu et al., 2019), the concentration of FSA···H₂O is 1.36×10^6 - 6.80×10^6



181 molecules·cm⁻³ within 280.0-320.0 K, which is 10⁶ times larger than that of SO₃·H₂O (Table S3).
182 Therefore, it is predicted that SO₃ hydrolysis with FSA predominantly take places via the collision
183 between FSA·H₂O and SO₃.

184 Starting from the FSA·H₂O + SO₃ reactants, an eight-membered ring pre-reactive complex
185 SO₃·H₂O·FSA (named as IM_{SA_FSA}) was found and its Gibbs free energy relative to the isolated
186 SO₃, H₂O and FSA reactants was -2.0 kcal·mol⁻¹. In comparison to the previously reported neutral
187 (SO₃·2H₂O) and acidic complexes SO₃·H₂O·X (X = HNO₃, HCOOH, (COOH)₂ and H₂SO₄)
188 (Yang et al., 2021; Long et al., 2012; Torrent-Sucarrat et al., 2012; Long et al., 2013), the stability
189 of the SO₃·H₂O·FSA complex is notably enhanced by 0.2-2.7 kcal·mol⁻¹. This is because the
190 positive electrostatic potential (ESP) of the hydrogen atom in the FSA molecule (Fig. S4) is stronger
191 than those in H₂O and X molecules, resulting in stronger intermolecular interactions of
192 SO₃·H₂O·FSA. Following the IM_{SA_FSA} complex, the reaction proceeds via TS_{SA_FSA}, leading to
193 the H₂SO₄·FSA formation. For the FSA-catalyzed SO₃ hydrolysis, its Gibbs free energy barrier is
194 2.5 kcal·mol⁻¹, representing a reduction of 22.1 kcal·mol⁻¹ relative to the SO₃ hydrolysis without
195 FSA (Table S1). Moreover, it is also 1.0-4.0 kcal·mol⁻¹ lower in free energy barrier than those of
196 the SO₃ hydrolysis with H₂O, HNO₃ and H₂SO₄ (Table S1). Therefore, FSA is clearly more effective
197 than H₂O, HNO₃ and H₂SO₄ in decreasing the energy barrier for SO₃ hydrolysis. H₂SO₄·FSA is
198 an eight-membered ring complex, similar to H₂SO₄·X complexes in the SO₃ hydrolysis with X.
199 The predicted free energy of H₂SO₄·FSA (-12.9 kcal·mol⁻¹) is lower by 10.9 kcal·mol⁻¹ compared
200 to that of the IM_{SA_FSA} complex. This indicates the thermodynamic favorability of FSA-assisted SO₃
201 hydrolysis.

202 The computed rate coefficients for the hydrolysis of SO₃ with and without FSA, H₂O and X
203 within 280.0-320.0 K are shown in Table 1. As observed at 298.0 K, the rate coefficient for the SO₃
204 hydrolysis with FSA (k_{FSA}) is 7.71×10^{-11} cm³·molecule⁻¹·s⁻¹, surpassing that of the uncatalyzed
205 SO₃ hydrolysis by a factor of 10¹². Additionally, the value of k_{FSA} at 298.0 K is larger by factors of
206 60.23 and 84.63 than those for the SO₃ hydrolysis with H₂O (k_{WM}) and HNO₃ (k_{NA}), respectively.
207 Similarly, within 280.0-320.0 K in Table 1, FSA can compete with HCOOH, (COOH)₂ and H₂SO₄
208 with the value of k_{FSA} being larger by factors of 1.02-1.64 than those of k_{FA} , k_{OA} and k_{SA} . These
209 findings indicate that the catalytic efficiency of FSA in SO₃ hydrolysis surpasses that of H₂O and
210 HNO₃, and is comparable to HCOOH, (COOH)₂ and H₂SO₄.



211 To consider a contribution of FSA on SO₃ hydrolysis, the rate ratios between FSA- and X-
212 catalyzed SO₃ hydrolysis reactions were calculated, as shown in Table S5. As observed, the SO₃
213 hydrolysis with H₂O is more favorable than with FSA because the [H₂O] (10¹⁶-10¹⁸ molecules·cm⁻³)
214 is significantly greater than [FSA] (10⁷ molecules·cm⁻³). When the acid catalysts HNO₃ (10⁹
215 molecules·cm⁻³), HCOOH (10⁸ molecules·cm⁻³) and SA (10⁶ molecules·cm⁻³) are considered, FSA
216 dominates over them within 280.0-320.0 K as the rate ratio v_{WM}/v_X is greater than 1. This reveals
217 that the FSA-assisted reaction is indispensable in SO₃ hydrolysis within regions affected by FSA
218 pollution and can significantly promote the hydrolysis of SO₃ within 280.0-320.0 K.

219 3.2 FSA-Catalyzed SO₃ Hydrolysis at the Gas-liquid Nanodroplet Interface

220 Aqueous interfaces are widespread across Earth's atmosphere. (Li et al., 2024a; Zhong et al.;
221 2017; Sun et al., 2024; Gao et al., 2024; Dong et al., 2024). The gas-liquid nanodroplet interface
222 serves as a significant site for adsorption and reactions, potentially enhancing atmospheric reaction
223 rates and leading to the emergence of novel mechanisms. However, at the gas-liquid nanodroplet
224 interface, comprehensive understanding of the mechanism for FSA-assisted SO₃ hydrolysis was
225 lacking. Notably, during the 150 ns simulation, SO₃, the FSA molecule and the SO₃-FSA complex
226 were observed to reside at the interface for 35.8%, 46.3% and 40.5% (Fig. S5), respectively,
227 revealing that the presence of SO₃, FSA molecule and SO₃-FSA complex cannot be ignored at the
228 gas-liquid nanodroplet interface. To further investigate this prediction, we performed BOMD
229 simulations to assess the FSA-assisted hydrolysis of SO₃ at the gas-liquid nanodroplet interface.
230 Similar to the reactions of SO₃ with other acidic species at this interface, the interaction between
231 SO₃ and FSA at the aqueous interface might take place via three pathways: (i) direct interaction of
232 SO₃ with adsorbed FSA; (ii) interaction of adsorbed SO₃ with FSA; or (iii) reaction starting from
233 the SO₃-FSA complex. Given the high reactivity and the brief residency time of SO₃ and FSA at the
234 interface, as evidenced by their short lifetimes (Fig. S6) of only a few picoseconds and rapid
235 formation of SA⁻ and FSA⁻ ion, the simulations have primarily considered the model of (iii). This
236 focus enabled a deeper understanding of the interfacial dynamics and the mechanisms underpinning
237 these rapid transformations.

238 Unlike the gaseous hydrolysis mechanism of SO₃ with FSA, which occurs through the one-
239 step mechanism, interfacial SO₃ hydrolysis mediated by FSA occurs via a stepwise mechanism (Fig.
240 2, Fig. S7 and Movie S1), consisting of three steps: i) SO₃ hydrolysis along with proton transfer



241 outside the ring; *ii*) the deprotonation of FSA; and *iii*) the deprotonation of H₂SO₄. Specifically, at
242 0 ps, a loop-structure complex, SO₃···(H₂O)₂···FSA, was initially found with the formations of three
243 hydrogen bonds ($d_{(O6\cdots H4)} = 1.75$; $d_{(O3\cdots H2)} = 1.92$ and $d_{(O5\cdots H3)} = 2.39$ Å) and a van der Waals
244 interaction ($d_{(O1\cdots S)} = 2.31$ Å). Then, the loop structure mechanism proceeded along with the
245 simultaneous event of the proton transfer outside the ring. At 1.01 ps, an arrangement resembling a
246 transition state was found for the interfacial SO₃ hydrolysis, characterized by shortening of the S-
247 O1 and O2-H1 bonds and elongation of the O1-H1 bond. By 1.14 ps, the S-O1 and O2-H1 bond
248 lengths had reduced to 1.45 Å and 0.97 Å, respectively, while the O1-H1 bond had elongated to
249 1.42 Å, indicating the formation of HSO₄⁻ and H₃O⁺ ions. Due to the strong acidity of FSA, the H3
250 atom of FSA was moved to the O5 atom of the HSO₄⁻ ion at 1.87 ps, leading to H₂SO₄ molecule and
251 FSA⁻ ion. Finally, the deprotonation of H₂SO₄ was completed at 2.18 ps, with the H2 atom of H₂SO₄
252 moved to one interfacial water molecule inside the ring. In contrast to the SO₃ hydrolysis with FSA
253 in the gas phase, which does not proceed within 100 ps, the reaction at the gas-liquid nanodroplet
254 interface rapidly proceeds within just a few picoseconds. This indicates that interfacial water
255 molecules at the gas-liquid nanodroplet interface can accelerate the SO₃ hydrolysis.

256 Interestingly, the formation of FSA⁻ and HSO₄⁻ is highly stable, and their dissociation did not
257 occur within 10 ps. Species such as H₂SO₄ (SA), NH₃ (A), HNO₃, and (COOH)₂ are identified as
258 candidates for particle formation, with the SA-A cluster serving as a significant precursor to
259 atmospheric aerosols. Calculated binding free energies of the corresponding bimolecular clusters
260 were shown in Table 2 where the computed binding free energies agree well with previous values
261 (Zhong et al., 2019). As shown, the interactions of FSA⁻-SA (-21.2 kcal·mol⁻¹) and FSA⁻-HNO₃ (-
262 12.1 kcal·mol⁻¹) are stronger than that of SA-A (-8.9 kcal·mol⁻¹), illustrating that interfacial FSA⁻
263 and H₃O⁺ ions can attract precursor molecules from the gaseous phase to the aqueous nanodroplet
264 surface, and thus facilitating particle growth. Additionally, the enhancing potential of the FSA⁻ ion
265 on the SA-A cluster was assessed by examining the binding free energies of the SA-A-FSA⁻ and
266 SA-A-*Y* (*Y* = HOOCCH₂COOH, HOCCOOSO₃H, CH₃OSO₃H, HOOCCH₂CH(NH₂)COOH and
267 HOCH₂COOH) clusters. The binding free energies of SA-A-FSA⁻ and SA-A-*Y* clusters listed in
268 Table 2 were consistent with previously reported values (Rong et al., 2020; Zhang et al., 2018;
269 Zhang et al., 2017; Gao et al., 2023; Liu et al., 2021a). Notably, compared to SA-A-*Y*, the binding
270 free energy of SA-A-FSA⁻ (-25.6 kcal·mol⁻¹) was larger than 5.2-12.8 kcal·mol⁻¹, indicating that the



271 FSA⁻ at the interface exhibits a greater nucleation capability than gaseous molecule *Y*. Consequently,
272 FSA⁻ is expected to demonstrate enhanced nucleation potential at the gas-liquid interface.

273 **3.3 FSA's Role in Nucleation and Cluster Formation**

274 Electrostatic potential (ESP) analysis was conducted to predict the potential hydrogen bond
275 binding sites among FSA, SA and A. The -OH moiety in the FSA molecule contains a highly
276 electrophilic hydrogen atom, making it a favorable donor site for hydrogen bonds (ESP value: +60.6
277 kcal·mol⁻¹) (Fig. 3). Meanwhile, the terminal oxygen atoms of the -SO₃H and -COOH moieties in
278 FSA can act as an effective hydrogen bond receptor site due to their stronger electronegativity (ESP
279 values: -23.8, -22.4 and -13.0 kcal·mol⁻¹). Thus, FSA can form stable clusters by forming hydrogen
280 bonds with SA and A.

281 Using MD simulations, the aggregation behavior of FSA with SA and A molecules was
282 investigated at various atmospheric temperatures (Fig. 4 and Figs. S8-S9). In these simulation
283 systems, 5 FSA, 5 SA, 10 A, 20 H₂O, 41 O₂ and 154 N₂ molecules were included. Notably, the
284 complete stable (FSA)₅·(SA)₅·(A)₁₀ cluster was observed at all the three simulations temperatures.
285 With rising temperatures, the aggregation time for the formation of (FSA)₅·(SA)₅·(A)₁₀ cluster (Fig.
286 4(a)) increases. This observed phenomenon of aggregation implies that lower temperatures are more
287 conducive to form the (FSA)₅·(SA)₅·(A)₁₀ cluster. Fig. 4(b) displayed the snapshots of the nucleation
288 simulation at 258.15 K. The initial simulation at 0 ns shows that there is not effective nucleation, as
289 all molecules in the system are scattered (Fig. 4(b)). Subsequently, FSA can bind with SA and A to
290 form FSA·A, FSA·SA·A and FSA·SA·(A)₃ clusters at 1.5 ns, and then the FSA·SA·A,
291 (FSA)₂·SA·(A)₃ and (FSA)₂·(SA)₂·(A)₃ clusters are formed at 3.0 ns. Next, with further aggregation
292 of FSA molecules, (FSA)₂·SA·(A)₄ and (FSA)₃·(SA)₃·(A)₄ clusters are observed within 4.0 ns.
293 Finally, the FSA molecules fully aggregate to form (FSA)₅·(SA)₅·(A)₁₀ clusters at 7.5 ns, and this
294 complete cluster stays stable throughout the entire simulation period. It is noteworthy that the
295 numbers of FSA molecules can gradually interact with SA and A molecules to form relatively large
296 clusters, where hydrogen bonds among SA, A and FSA play a crucial role. Therefore, it is initially
297 predicted that FSA could act as a “participator” in NPF and could be directly involved in SA-A
298 nucleation. Further predictions regarding for the enhancement effect of FSA on SA-A molecular
299 clustering have been studied by considering the cluster stability, the formation rate and the growth
300 pathways.



301 **3.4 The Impact of Atmospheric Conditions on the Thermodynamic Clusters** 302 **Stability**

303 The Gibbs free energies of formation (ΔG , kcal·mol⁻¹) and evaporation rate coefficients (γ , s⁻¹)
304 of the (FSA)_x(SA)_y(A)_z clusters were analyzed to estimate the thermodynamic stability of the
305 clusters involved in the SA-A-FSA system (Tables S6-S7). The ΔG and γ of the important pure
306 SA·A clusters and FSA-containing stable clusters were primarily discussed at three temperature. At
307 298.15 K, the ΔG value of the SA·A cluster was 2.1 kcal·mol⁻¹ greater than that of the FSA·A cluster
308 (Fig. 5). Meanwhile, its γ value was about 10 times greater than that of the FSA·A cluster, suggesting
309 that the FSA·A cluster is more stable and likely to participate in subsequent growth as an initial
310 cluster. For the (FSA)₂·(A)₂ cluster, its ΔG (-31.1 kcal·mol⁻¹) was smaller by 4.6 kcal·mol⁻¹ than that
311 of the (SA)₂·(A)₂ cluster (-26.5 kcal·mol⁻¹) with the γ value of the former one (5.34×10^1 s⁻¹) at least
312 10⁴ times lower than that of the latter one (6.13×10^5 s⁻¹), indicating that the (FSA)₂·(A)₂ cluster is
313 more stable than clusters containing SA and A with the same acid-base number. For the (FSA)₃·(A)₃
314 cluster, its γ (3.30×10^1 s⁻¹) was nearly 10³ times lower than that of the (SA)₃·(A)₃ (2.25×10^2 s⁻¹)
315 cluster, allowing (FSA)₃·(A)₃ to serve as a critical nucleation cluster and participate in subsequent
316 growth. Similarly, at 278.15 K and 258.15 K, the FSA·A, (FSA)₂·(A)₂ and (FSA)₃·(A)₃ clusters
317 were all more stable than the SA-A binary nucleation clusters with the same acid-base number.
318 Regarding for the (FSA)₂·SA·(A)₃ and FSA·(SA)₂·(A)₃ clusters at 298.15 K, the ΔG values (-56.7
319 and -54.1 kcal·mol⁻¹) were lower than that of (SA)₃·(A)₃ (-52.0 kcal·mol⁻¹). Simultaneously, the γ
320 values of the (FSA)₂·SA·(A)₃ (8.49×10^{-4} s⁻¹) and FSA·(SA)₂·(A)₃ (5.75×10^1 s⁻¹) clusters were
321 respectively lower 10⁶ and 10 times lower than that of (SA)₃·(A)₃ (2.25×10^2 s⁻¹). Likewise, the
322 (FSA)₂·SA·(A)₃ and FSA·(SA)₂·(A)₃ clusters were more stable than the (SA)₃·(A)₃ cluster at low
323 temperatures (278.15 K and 258.15 K) due to their significantly lower evaporation rates. Therefore,
324 compared to pure SA-A clusters, clusters containing FSA molecules exhibit higher stability and are
325 more likely to engage in nucleation and subsequent cluster growth processes as stable clusters. The
326 clusters of (SA)₃·(A)₃, (FSA)₂·SA·(A)₃ and FSA·(SA)₂·(A)₃ have the potential to further grow into
327 the boundary clusters [(FSA)₂·(SA)₂·(A)₃, (FSA)₁·(SA)₃·(A)₃, (SA)₄·(A)₃ and (SA)₄·(A)₄].

328 **3.5 Influence of Particle Formation Rates Under Varying Temperatures and** 329 **Nucleation Precursor Concentrations**

330 To investigate the cluster formation rate (J , cm⁻³·s⁻¹) and the enhancement factor (R) of cluster



331 formation rate by FSA, a range of ACDC simulations were performed using thermodynamic data
332 for the SA-A-FSA clusters at varying temperatures and monomer concentrations ($[SA] = 10^4 - 10^8$,
333 $[A] = 10^7 - 10^{11}$ and $[FSA] = 10^3 - 10^7$ molecules \cdot cm $^{-3}$). The value of R is defined as $R = J_{SA-A-FSA} / J_{SA-A}$.
334 The values of J and R for the SA-A-FSA system at varying temperatures (Fig. 6) showed that J
335 increased as the temperature decreased, due to the smaller values of both ΔG and γ at lower
336 temperatures. Meanwhile, J increased with increasing $[FSA]$, attributable to the formation of more
337 SA-A-FSA clusters. Variations in $[FSA]$ and temperature can also affect R . A significant increase in
338 R with the rising $[FSA]$ has been observed, suggesting that FSA can strongly enhance the nucleation
339 rate in SA-A NPF. Interestingly, as the temperature increases (Fig. 6(b)), the value of R becomes
340 greater. In summary, the inclusion of FSA can substantially improve J for SA-A nucleation in
341 regions with relatively high $[FSA]$ during summer or at lower altitudes with high temperatures.

342 In addition to temperature and $[FSA]$, J and R can also be affected by $[SA]$ and $[A]$. At 278.15
343 K, J increased with increase of $[SA]$ or $[A]$ (Fig. 7(a)). Nevertheless, R decreased with increasing
344 $[SA]$ (Fig. 7(b)). This trend may be due to both FSA and SA are acidic molecules, creating a
345 competitive relationship when they interact with A. Additionally, the changes in J with $[SA]$ or $[A]$
346 and R with $[SA]$ were similar at other temperatures of 258.15 K and 298.15 K. Similar negative
347 dependencies between R and $[A]$ were observed at both 278.15 K and 298.15 K. This occurs because,
348 as the $[A]$ increases, the interaction between FSA and SA in the SA-A-FSA system may be disrupted,
349 leading to a decrease in the saturation of FSA interaction sites and a reduction in R . Notably, at the
350 lower temperature of 258.15 K, when $[FSA]$ was high, the value of R initially decreased and then
351 increased with increasing $[A]$ (as depicted in Fig. S12 (b)). This may be attributed to the following
352 reasons. First, as $[A]$ increases, the interaction between FSA and SA in the ternary cluster may be
353 disrupted, leading to a decrease in the saturation of FSA interaction sites and a reduction in R . Then,
354 as the concentration of A further increases, excess A molecules bind to FSA molecules, leading to
355 an increase in R . In summary, FSA primarily enhances SA-A nucleation in regions with higher
356 temperatures and lower $[A]$ and $[SA]$.

357 3.6 FSA-Driven Nucleation Enhancement Mechanism

358 The clusters formed in the system via two main pathways: the pure SA-A pathway and SA-A-
359 FSA pathways (Fig. 8). The pure SA-A nucleation pathway primarily formed stable $(SA)_3 \cdot (A)_3$
360 clusters through monomer addition and collision with SA \cdot A cluster. The SA-A-FSA nucleation



361 pathway can be categorized into two routes. One route involved the initial formation of the stable
362 cluster $\text{FSA}\cdot\text{A}$, which then collided with one SA molecule, an FSA molecule, or another $\text{FSA}\cdot\text{A}$
363 cluster to form subsequent stable clusters and continue growing. The other route involved the initial
364 formation of the stable $(\text{SA})_2\cdot\text{A}$ cluster, which then collided with one $\text{FSA}\cdot\text{A}$ cluster to form the
365 stable $(\text{SA})_2\cdot(\text{A})_2\cdot\text{FSA}$, continuing to grow through the addition of an A molecule or an FSA
366 molecule. Interestingly, at varying temperatures and concentrations of nucleating precursors, the
367 FSA molecule exhibited distinct effects and contributions in the SA-A system. As the temperature
368 increased, the contribution of the SA-A-FSA pathway rose from 51% to 97% (Fig. 9(a)). Therefore,
369 the cluster growth pathway involving FSA appears to prevail at relatively higher temperatures, such
370 as during summer or at lower altitudes. The involvement of FSA in the primary cluster formation
371 pathway may also be influenced by the concentration of the precursors. Specifically, the contribution
372 of the FSA participation pathway exhibited a negative correlation with $[\text{SA}]$ or $[\text{A}]$ at 278.15 K (Fig.
373 9(b-c)). Consequently, the contributions of the SA-A-FSA pathway may be more substantial in the
374 clean atmospheric boundary layer with low $[\text{A}]$ and $[\text{SA}]$, such as in area distant from heavy traffic
375 and emission sources of SA. Additionally, the contribution of the SA-A-FSA pathway increases as
376 $[\text{FSA}]$ rises (Fig. 9(d)). At low $[\text{FSA}]$ (10^3 molecules $\cdot\text{cm}^{-3}$), the contribution of SA-A-FSA pathway
377 was only 35%, with cluster growth pathways predominantly governed by the formation of pure SA-
378 A clusters. However, as $[\text{FSA}]$ increased to 10^4 molecules $\cdot\text{cm}^{-3}$, the contribution of FSA-involving
379 clusters rose to 84%, making the pathway involving FSA dominant for cluster formation in the SA-
380 A-FSA system. Moreover, the SA-A-FSA mechanism contributed more significantly (97%) at
381 higher $[\text{FSA}]$ concentrations (10^5 - 10^7 molecules $\cdot\text{cm}^{-3}$). In summary, consistent with the variation
382 observed in R with temperature and precursor concentrations, the contribution of the pathway
383 involving FSA is significantly dominant in the NPF process with decreasing $[\text{SA}]$ and $[\text{A}]$ and
384 increasing temperature and $[\text{FSA}]$. These results suggest that FSA could be a significant contributor
385 to SA-A atmospheric NPF, and the SA-A-FSA pathway may dominate in regions with high FSA
386 emissions and relatively high temperatures.

387 4. Summary and Conclusions

388 The potential contribution of FSA to gaseous and interfacial SO_3 hydrolysis, as well as its
389 enhancement of atmospheric particle formation was investigated. Gaseous results indicated that SO_3



390 hydrolysis with FSA has a Gibbs free energy barrier as low as $1.5 \text{ kcal}\cdot\text{mol}^{-1}$ and can effectively
391 compete with SO_3 hydrolysis by HNO_3 ($10^9 \text{ molecules}\cdot\text{cm}^{-3}$), HCOOH ($10^8 \text{ molecules}\cdot\text{cm}^{-3}$) and
392 H_2SO_4 ($10^6 \text{ molecules}\cdot\text{cm}^{-3}$) over a temperature range of 280.0-320.0 K. Interfacial BOMD
393 simulations illustrated that FSA-mediated SO_3 hydrolysis at the gas-liquid interface occurs through
394 a stepwise mechanism and can be completed within a few picoseconds. ACDC kinetic simulations
395 indicated that FSA significantly enhances cluster formation rates in the $\text{H}_2\text{SO}_4\text{-NH}_3$ system during
396 summer, increasing rates by more than 10^7 times under conditions of high FSA concentrations and
397 low H_2SO_4 and NH_3 levels. The $\text{H}_2\text{SO}_4\text{-NH}_3\text{-FSA}$ nucleation mechanism exhibits a stronger
398 nucleation ability than classical nucleation, making it a promising process for urban polluted
399 environments rich in FSA sources. Meanwhile, the interfacial species formed, such as HSO_4^- , H_3O^+
400 and FSA^- , act to attract precursor species (e.g., H_2SO_4 , NH_3 and HNO_3) from the gas phase to the
401 nanodroplet interface, thereby facilitating further particle growth. This study broadens our
402 understanding of a novel SO_3 hydrolysis pathway involving FSA in polluted regions, identifies
403 previously overlooked new particle formation (NPF) sources in industrial areas, and deepens
404 knowledge of the atmospheric organic-sulfur cycle.

405 **Acknowledgments**

406 This work was supported by the National Natural Science Foundation of China (No: 22203052;
407 22073059; 42107109); the Key Cultivation Project of Shaanxi University of Technology (No:
408 SLG2101); the Education Department of Shaanxi Provincial Government (No. 23JC023).

409 **Declaration of competing interest**

410 The authors declare that they have no known competing financial interests or personal
411 relationships that could have appeared to influence the work reported in this paper.

412 **Reference**

- 413 Abraham, M., Alekseenko, A., Basov, V., Bergh, C., Briand, E., Brown, A., Doijade, M., Fiorin, G.,
414 Fleischmann, S., Gorelov, S., Gouillardet, G., Grey, A., Irrgang, M. E., Jalalypour, F., Jordan,
415 J., Kutzner, C., Lemkul, J. A., Lundborg, M., Merz, P., Miletic, V., Morozov, D., Nabet, J., Pall,
416 S., Pasquadibisceglie, A., Pellegrino, M., Santuz, H., Schulz, R., Shugaeva, T., Shvetsov, A.,
417 Villa, A., Wingbermuehle, S., Hess, B., Lindahl, E. GROMACS 2024.3 Manual.,
418 <https://doi.org/10.5281/zenodo.13457083>, 2024.
419 Bandyopadhyay, B., Kumar, P., and Biswas, P.: Ammonia catalyzed formation of sulfuric acid in
420 troposphere: The curious case of a base promoting acid rain, *J. Phys. Chem. A*, 121, 3101-3108,
421 <https://doi.org/10.1021/acs.jpca.7b01172>, 2017.



- 422 Bao, J. L., Zhang, X., and Truhlar, D. G.: Barrierless association of CF_2 and dissociation of C_2F_4 by
423 variational transition-state theory and system-specific quantum Rice-Ramsperger-Kassel
424 theory, *Proc. Natl. Acad. Sci. U.S.A.*, 113, 13606-13611,
425 <https://doi.org/10.1073/pnas.1616208113>, 2016.
- 426 Becke, A. D.: Density-functional exchange-energy approximation with correct asymptotic behavior,
427 *Phys. Rev. A*, 38, 3098-3100, <https://doi.org/10.1103/physreva.38.3098>, 1988.
- 428 Berendsen, H. J. C., Postma, J. P. M., van Gunsteren, W. F., DiNola, A., and Haak, J. R.: Molecular
429 dynamics with coupling to an external bath, *J. Chem. Phys.*, 81, 3684-3690,
430 <https://doi.org/10.1063/1.448118>, 1984.
- 431 Bondybey, V. E., and English, J. H.: Infrared spectra of SO_3 polymers and complexes in rare gas
432 matrices, *J. Mol. Spectrosc.*, 109, 221-228, [https://doi.org/10.1016/0022-2852\(85\)90308-X](https://doi.org/10.1016/0022-2852(85)90308-X),
433 1985.
- 434 Bussi, G., Donadio, D., and Parrinello, M.: Canonical sampling through velocity rescaling, *J. Chem.*
435 *Phys.*, 126, 014101, <https://doi.org/10.1063/1.2408420>, 2007.
- 436 Carmona-García, J., Trabelsi, T., Francés-Monerris, A., Cuevas, C. A., Saiz-Lopez, A., Roca-
437 Sanjuán, D., and Francisco, J. S.: Photochemistry of HOSO_2 and SO_3 and implications for the
438 production of sulfuric acid, *J. Am. Chem. Soc.*, 143, 18794-18802,
439 <https://doi.org/10.1021/jacs.1c10153>, 2021.
- 440 Chen, T., and Plummer, P. L.: Ab initio MO investigation of the gas-phase reaction sulfur trioxide +
441 water. *faradw. sulfuric acid*, *J. Phys. Chem.*, 89, 3689-3693,
442 <https://doi.org/10.1021/j100263a023>, 1985.
- 443 Cheng, Y., Ding, C., Zhang, T., Wang, R., Mu, R., Li, Z., Li, R., Shi, J., and Zhu, C.: Barrierless
444 reactions of C_2 Criegee intermediates with H_2SO_4 and their implication to oligomers and new
445 particle formation, *J. Environ. Sci.*, 149, 574-584, <https://doi.org/10.1016/j.jes.2023.12.020>,
446 2025.
- 447 Couling, S. B., Sully, K. J., and Horn, A. B.: Experimental study of the heterogeneous interaction
448 of SO_3 and H_2O : formation of condensed phase molecular sulfuric acid hydrates, *J. Am. Chem.*
449 *Soc.*, 125, 1994-2003, <https://doi.org/10.1021/ja0210704>, 2003.
- 450 Dong, Z., Francisco, J. S., and Long, B.: Ammonolysis of glyoxal at the air-water nanodroplet
451 interface, *Angew. Chem. Int. Ed.*, 63, e202316060, <https://doi.org/10.1002/anie.202316060>,
452 2024.
- 453 Fang, Y.-G., Wei, L., Francisco, J. S., Zhu, C., and Fang, W.-H.: Mechanistic insights into chloric
454 acid production by hydrolysis of chlorine trioxide at an air-water interface, *J. Am. Chem. Soc.*,
455 146, 21052-21060, <https://doi.org/10.1021/jacs.4c06269>, 2024.
- 456 Feng, Y., and Wang, C.: Surface Confinement of finite-size water droplets for SO_3 hydrolysis
457 reaction revealed by molecular dynamics simulations based on a machine learning force field,
458 *J. Am. Chem. Soc.*, 145, 10631-10640, <https://doi.org/10.1021/jacs.3c00698>, 2023.
- 459 Fleig, D. G., Vainio, E., Andersson, K., Brink, A., Johnsson, F., and Hupa, M.: Evaluation of SO_3
460 measurement techniques in air and oxy-fuel combustion, *Energy Fuels*, 26, 5537-5549,
461 <https://doi.org/10.1021/EF301127X>, 2012.
- 462 Frisch, M. J., Trucks, G. W., Schlegel, H. B., Scuseria, G. E., Robb, M. A., Cheeseman, J. R.,
463 Scalmani, G., Barone, V., Mennucci, B., Petersson, G. A., Nakatsuji, H., Caricato, M., Li, X.,
464 Hratchian, H. P., Izmaylov, A. F., Bloino, J., Zheng, G., Sonnenberg, J. L., Hada, M., Ehara,
465 M., Toyota, K., Fukuda, R., Hasegawa, J., Ishida, M., Nakajima, T., Honda, Y., Kitao, O., Nakai,



- 466 H., Vreven, T., Montgomery, J. A., Jr., Peralta, J. E., Ogliaro, F., Bearpark, M., Heyd, J. J.,
467 Brothers, E., Kudin, K. N., Staroverov, V. N., Kobayashi, R., Normand, J., Raghavachari, K.,
468 Rendell, A., Burant, J. C., Iyengar, S. S., Tomasi, J., Cossi, M., Rega, N., Millam, J. M., Klene,
469 M., Knox, J. E., Cross, J. B., Bakken, V., Adamo, C., Jaramillo, J., Gomperts, R., Stratmann,
470 R. E., Yazyev, O., Austin, A. J., Cammi, R., Pomelli, C., Ochterski, J. W., Martin, R. L.,
471 Morokuma, K., Zakrzewski, V. G., Voth, G. A., Salvador, P., Dannenberg, J. J., Dapprich, S.,
472 Daniels, A. D., Farkas, Ö., Foresman, J. B., Ortiz, J. V., Cioslowski, J., and Fox, D. J.:
473 Gaussian09 Revision D. 01, Gaussian Inc. Wallingford CT, <http://www.gaussian.com>, 2009.
- 474 Gao, J., Wang, R., Zhang, T., Liu, F., and Wang, W.: Effect of methyl hydrogen sulfate on the
475 formation of sulfuric acid-ammonia clusters: A theoretical study, *J. Chin. Chem. Soc.*, 70, 689-
476 698, <https://doi.org/10.1002/jccs.202200148>, 2023.
- 477 Gao, Q., Dong, Z., and Long, B.: Reactions of sulfur trioxide with hypochlorous acid catalyzed by
478 water in gas phase and at the air-water nanodroplet interface in the atmosphere: An important
479 sink for hypochlorous acid, *Atmospheric Environ.*, 331, 120574,
480 <https://doi.org/10.1016/j.atmosenv.2024.120574>, 2024.
- 481 Glowacki, D. R., Liang, C. H., Morley, C., Pilling, M. J., and Robertson, S. H.: MESMER: an open-
482 source master equation solver for multi-energy well reactions, *J. Phys. Chem. A*, 116, 9545-
483 9560, <https://doi.org/10.1021/jp3051033>, 2012.
- 484 Goedecker, S., Teter, M., and Hutter, J.: Separable dual-space Gaussian pseudopotentials, *Phys. Rev.*
485 *B*, 54, 1703, <https://doi.org/10.1103/PhysRevB.54.1703>, 1996.
- 486 Grimme, S., Antony, J., Ehrlich, S., and Krieg, H.: A consistent and accurate ab initio
487 parametrization of density functional dispersion correction (DFT-D) for the 94 elements H-Pu,
488 *J. Chem. Phys.*, 132, 154104, <https://doi.org/10.1063/1.3382344>, 2010.
- 489 Hess, B., Bekker, H., Berendsen, H. J. C., and Fraaije, J. G. E. M.: LINCS: A linear constraint solver
490 for molecular simulations, *J. Comput. Chem.*, 18, 1463-1472,
491 [https://doi.org/10.1002/\(SICI\)1096-987X\(199709\)18:12<1463::AID-JCC4>3.0.CO;2-H](https://doi.org/10.1002/(SICI)1096-987X(199709)18:12<1463::AID-JCC4>3.0.CO;2-H),
492 1997.
- 493 Hutter, J., Iannuzzi, M., Schiffmann, F., and VandeVondele, J.: cp2k: atomistic simulations of
494 condensed matter systems, *Wiley Interdiscip. Rev. Comput. Mol. Sci.*, 4, 15-25,
495 <https://doi.org/10.1002/wcms.1159>, 2014.
- 496 Kangas, P., Hänninen, V., and Halonen, L.: An ab initio molecular dynamics study of the hydrolysis
497 reaction of sulfur trioxide catalyzed by a formic acid or water molecule, *J. Phys. Chem. A*, 124,
498 1922-1928, <https://doi.org/10.1021/acs.jpca.9b11954>, 2020.
- 499 Kumar, A., Mallick, S., and Kumar, P.: Oxidation of HOSO[•] by Cl⁻: a new source of SO₂ in the
500 atmosphere?, *Phys. Chem. Chem. Phys.*, 23, 18707-18711,
501 <https://doi.org/10.1039/D1CP01048D>, 2021..
- 502 Kumar, A., Iyer, S., Barua, S., Brean, J., Besic, E., Seal, P., Dall'Osto, M., Beddows, D. C. S.,
503 Sarnela, N., Jokinen, T., Sipilä, M., Harrison, R. M., and Rissanen, M.: Direct measurements
504 of covalently bonded sulfuric anhydrides from gas-phase reactions of SO₃ with acids under
505 ambient conditions, *J. Am. Chem. Soc.*, 146, 15562-15575,
506 <https://doi.org/10.1021/jacs.4c04531>, 2024.
- 507 Lee, C., Yang, W., and Parr, R. G.: Development of the Colle-Salvetti correlation-energy formula
508 into a functional of the electron density, *Phys. Rev. B*, 37, 785-789,
509 <https://doi.org/10.1103/PHYSREVB.37.785>, 1988.



- 510 Li, H., Zhong, J., Vehkamäki, H., Kurtén, T., Wang, W., Ge, M., Zhang, S., Li, Z., Zhang, X.,
511 Francisco, J. S., and Zeng, X. C.: Self-Catalytic reaction of SO₃ and NH₃ to produce sulfamic
512 acid and its implication to atmospheric particle formation, *J. Am. Chem. Soc.*, 140, 11020-
513 11028, <https://doi.org/10.1021/jacs.8b04928>, 2018.
- 514 Li, M., Li, L., Liu, S., Zhang, Q., Wang, W., and Wang, Q.: Insights into the catalytic effect of
515 atmospheric organic trace species on the hydration of Criegee intermediates, *Sci. Total.
516 Environ.*, 949, 174877, <https://doi.org/10.1016/j.scitotenv.2024.174877>, 2024a.
- 517 Li, M., Zhang, Y., Yu, X., Li, L., Wang, S., Zhang, Q., Wang, W., and Wang, Q.: Mechanistic insights
518 into Criegee intermediates with benzoic acid at gas-phase and air-water interface and
519 nucleation of product, *Atmospheric Environ.*, 320, 120338,
520 <https://doi.org/10.1016/j.atmosenv.2024.120338>, 2024b.
- 521 Liu, J., Liu, L., Rong, H., and Zhang, X.: The potential mechanism of atmospheric new particle
522 formation involving amino acids with multiple functional groups, *Phys. Chem. Chem. Phys.*,
523 23, 10184-10195, <https://doi.org/10.1039/DOCP06472F>, 2021a.
- 524 Liu, L., Zhong, J., Vehkamäki, H., Kurtén, T., Du, L., Zhang, X., Francisco, J. S., and Zeng, X. C.:
525 Unexpected quenching effect on new particle formation from the atmospheric reaction of
526 methanol with SO₃, *Proc. Natl. Acad. Sci. U.S.A.*, 116, 24966-24971,
527 <https://doi.org/10.1073/pnas.1915459116>, 2019.
- 528 Liu, L., Yu, F., Tu, K., Yang, Z., and Zhang, X.: Influence of atmospheric conditions on the role of
529 trifluoroacetic acid in atmospheric sulfuric acid-dimethylamine nucleation, *Atmos. Chem.
530 Phys.*, 21, 6221-6230, <https://doi.org/10.5194/acp-21-6221-2021>, 2021b.
- 531 Long, B., Long, Z. W., Wang, Y. B., Tan, X. F., Han, Y. H., Long, C. Y., Qin, S. J., and Zhang, W. J.:
532 Formic acid catalyzed gas-phase reaction of H₂O with SO₃ and the reverse reaction: A
533 theoretical study, *ChemPhysChem*, 13, 323-329, <https://doi.org/10.1002/cphc.201100558>,
534 2012.
- 535 Long, B., Chang, C.-R., Long, Z.-W., Wang, Y.-B., Tan, X.-F., and Zhang, W.-J.: Nitric acid
536 catalyzed hydrolysis of SO₃ in the formation of sulfuric acid: A theoretical study, *Chem. Phys.
537 Lett.*, 581, 26-29, <https://doi.org/10.1016/j.cplett.2013.07.012>, 2013.
- 538 Long, B., Xia, Y., Bao, J. L., Carmona-García, J., Gómez Martín, J. C., Plane, J. M. C., Saiz-Lopez,
539 A., Roca-Sanjuán, D., and Francisco, J. S.: Reaction of SO₃ with HONO₂ and implications for
540 sulfur partitioning in the atmosphere, *J. Am. Chem. Soc.*, 144, 9172-9177,
541 <https://doi.org/10.1021/jacs.2c03499>, 2022.
- 542 Lu, T., and Chen, F.: Multiwfn: A multifunctional wavefunction analyzer, *J. Comput. Chem.*, 33,
543 580-592, <https://doi.org/10.1002/jcc.22885>, 2012.
- 544 Lu, T.: Sobtop, Version 1.0, <http://sobereva.com/soft/Sobtop/>, 2023.
- 545 Lv, G., Sun, X., Zhang, C., and Li, M.: Understanding the catalytic role of oxalic acid in SO₃
546 hydration to form H₂SO₄ in the atmosphere, *Atmos. Chem. Phys.*, 19, 2833-2844,
547 <https://doi.org/10.5194/acp-19-2833-2019>, 2019.
- 548 Ma, X., Zhao, X., Huang, Z., Wang, J., Lv, G., Xu, F., Zhang, Q., and Wang, W.: Determination of
549 reactions between Criegee intermediates and methanesulfonic acid at the air-water interface,
550 *Sci. Tot. Environ.*, 707, 135804, <https://doi.org/10.1016/j.scitotenv.2019.135804>, 2020.
- 551 Mackenzie, R. B., Dewberry, C. T., and Leopold, K. R.: Gas phase observation and microwave
552 spectroscopic characterization of formic sulfuric anhydride, *Science*, 349, 58-61,
553 <https://doi.org/10.1126/science.aaa9704>, 2015.



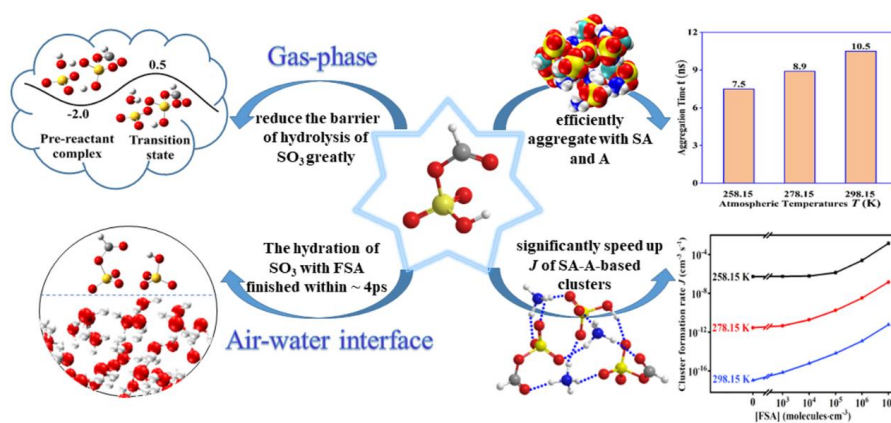
- 554 Martínez, L., Andrade, R., Birgin, E. G., and Martínez, J. M.: PACKMOL: A package for building
555 initial configurations for molecular dynamics simulations, *J. Comput. Chem.*, 30, 2157-2164,
556 <https://doi.org/10.1002/jcc.21224>, 2009.
- 557 Martins-Costa, M. T., and Ruiz-López, M. F.: The structure of carbon dioxide at the air-water
558 interface and its chemical implications, *Chem. Eur. J.* 30, e202400825,
559 <https://doi.org/10.1002/chem.202400825>, 2024.
- 560 McGrath, M. J., Olenius, T., Ortega, I. K., Loukonen, V., Paasonen, P., Kurtén, T., Kulmala, M., and
561 Vehkamäki, H.: Atmospheric Cluster Dynamics Code: a flexible method for solution of the
562 birth-death equations, *Atmos. Chem. Phys.*, 12, 2345-2355, [https://doi.org/10.5194/acp-12-
563 2345-2012](https://doi.org/10.5194/acp-12-2345-2012), 2012.
- 564 Meana-Pañeda, R., Zheng, J., Bao, J. L., Zhang, S., Lynch, B. J., Corchado, J. C., Chuang, Y.-Y.,
565 Fast, P. L., Hu, W.-P., Liu, Y.-P., Lynch, G. C., Nguyen, K. A., Jackels, C. F., Fernández-Ramos,
566 A., Ellingson, B. A., Melissas, V. S., Villà, J., Rossi, I., Coitiño, E. L., Pu, J., Albu, T. V., Zhang,
567 R. M., Xu, X., Ratkiewicz, A., Steckler, R., Garrett, B. C., Isaacson, A. D., and Truhlar, D. G.:
568 Polyrate 2023: A computer program for the calculation of chemical reaction rates for
569 polyatomics. New version announcement, *Comput. Phys. Commun.*, 294, 108933,
570 <https://doi.org/10.1016/j.cpc.2023.108933>, 2024.
- 571 Morokuma, K., and Muguruma, C.: Ab initio molecular orbital study of the mechanism of the gas
572 phase reaction $\text{SO}_3 + \text{H}_2\text{O}$: Importance of the second water molecule, *J. Am. Chem. Soc.*, 116,
573 10316-10317, <https://doi.org/10.1021/JA00101A068>, 1994.
- 574 Neese, F.: The ORCA program system, *WIREs Comput. Mol. Sci.*, 2, 73-78,
575 <https://doi.org/10.1002/wcms.81>, 2012.
- 576 Partanen, L., Vehkamäki, H., Hansen, K., Elm, J., Henschel, H., Kurtén, T., Halonen, R., and
577 Zapadinsky, E.: Effect of conformers on free energies of atmospheric complexes, *J. Phys.
578 Chem. A*, 120, 8613-8624, <https://doi.org/10.1021/acs.jpca.6b04452>, 2016.
- 579 Phillips, J. C., Braun, R., Wang, W., Gumbart, J., Tajkhorshid, E., Villa, E., Chipot, C., Skeel, R. D.,
580 Kalé, L., and Schulten, K.: Scalable molecular dynamics with NAMD, *J. Comput. Chem.*, 26,
581 1781-1802, <https://doi.org/10.1002/jcc.20289>, 2005.
- 582 Reiner, T., and Arnold, F.: Laboratory flow reactor measurements of the reaction $\text{SO}_3 + \text{H}_2\text{O} + \text{M}$
583 $\rightarrow \text{H}_2\text{SO}_4 + \text{M}$: Implications for gaseous H_2SO_4 and aerosol formation in the plumes of jet
584 aircraft, *J. Geophys. Res.*, 20, 2659-2662, <https://doi.org/10.1029/93GL02996>, 1993.
- 585 Rong, H., Liu, L., Liu, J., and Zhang, X.: Glyoxylic sulfuric anhydride from the gas-phase reaction
586 between glyoxylic acid and SO_3 : A potential nucleation precursor, *J. Phys. Chem. A*, 124, 3261-
587 3268, <https://doi.org/10.1021/acs.jpca.0c01558>, 2020.
- 588 Sarkar, S., Oram, B. K., and Bandyopadhyay, B.: Influence of ammonia and water on the fate of
589 sulfur trioxide in the troposphere: Theoretical investigation of sulfamic acid and sulfuric acid
590 formation pathways, *J. Phys. Chem. A*, 123, 3131-3141,
591 <https://doi.org/10.1021/acs.jpca.8b09306>, 2019.
- 592 Smith, C. J., Huff, A. K., Ward, R. M., and Leopold, K. R.: Carboxylic sulfuric anhydrides, *J. Phys.
593 Chem. A*, 124, 601-612, <https://doi.org/10.1126/science.1180315>, 2020.
- 594 Sun, G., Li, H., Hou, J., Wang, H., Wang, J., Lu, Z., and Gao, X.: Molecular behavior of ethylene
595 glycol/1,2-Butanediol Mixtures at the vapor-liquid interface, *Ind. Eng. Chem. Res.*, 63, 4853-
596 4865, <https://doi.org/10.1021/acs.iecr.3c03410>, 2024.



- 597 Tan, S., Zhang, X., Lian, Y., Chen, X., Yin, S., Du, L., and Ge, M.: OH group orientation leads to
598 organosulfate formation at the liquid aerosol surface, *J. Am. Chem. Soc.*, 144, 16953-16964,
599 <https://doi.org/10.1021/jacs.2c05807>, 2022.
- 600 Tang, B., Bai, Q., Fang, Y.-G., Francisco, J. S., Zhu, C., and Fang, W.-H.: Mechanistic insights into
601 N₂O₅-Halide ions chemistry at the air-water interface, *J. Am. Chem. Soc.*, 146, 21742-21751,
602 <https://doi.org/10.1021/jacs.4c05850>, 2024.
- 603 Tao, E. L., Li, J. Y., Soriano, S., and Tao, F.-M. J. C. J. o. C. P.: Quantum chemical study of potential
604 energy surface in the formation of atmospheric sulfuric acid, *Chin. J. Chem. Phys.* 31, 503-509,
605 <https://doi.org/10.1063/1674-0068/31/cjcp1805126>, 2018.
- 606 Torrent-Sucarrat, M., Francisco, J. S., and Anglada, J. M.: Sulfuric acid as autocatalyst in the
607 formation of sulfuric acid, *J. Am. Chem. Soc.*, 134, 20632-20644,
608 <https://doi.org/10.1021/ja307523b>, 2012.
- 609 Venkataraman, C., Mehra, A., and Mhaskar, P.: Mechanisms of sulphate aerosol production in
610 clouds: effect of cloud characteristics and season in the Indian region, *Tellus B*, 53, 260-272,
611 <https://doi.org/10.3402/tellusb.v53i3.16595>, 2001.
- 612 Wan, Z., Zhu, C., and Francisco, J. S.: Molecular insights into the spontaneous generation of Cl₂O
613 in the reaction of ClONO₂ and HOCl at the air-water interface, *J. Am. Chem. Soc.*, 145, 17478-
614 17484, <https://doi.org/10.1021/jacs.3c06527>, 2023.
- 615 Wang, R., Cheng, Y., Chen, S., Li, R., Hu, Y., Guo, X., Zhang, T., Song, F., and Li, H.: Reaction of
616 SO₃ with H₂SO₄ and its implications for aerosol particle formation in the gas phase and at the
617 air-water interface, *Atmos. Chem. Phys.*, 24, 4029-4046, [https://doi.org/10.5194/acp-24-4029-
618 2024](https://doi.org/10.5194/acp-24-4029-2024), 2024.
- 619 Yang, Y., Liu, L., Wang, H., and Zhang, X.: Molecular-Scale mechanism of sequential reaction of
620 oxalic acid with SO₃: Potential participator in atmospheric aerosol nucleation, *J. Phys. Chem.*
621 *A*, 125, 4200-4208, <https://doi.org/10.1021/acs.jpca.1c02113>, 2021.
- 622 Yao, L., Garmash, O., Bianchi, F., Zheng, J., Yan, C., Kontkanen, J., Junninen, H., Mazon, S. B.,
623 Ehn, M., Paasonen, P., Sipilä, M., Wang, M., Wang, X., Xiao, S., Chen, H., Lu, Y., Zhang, B.,
624 Wang, D., Fu, Q., Geng, F.-H., Li, L., Wang, H., Qiao, L., Yang, X., Chen, J., Kerminen, V.-
625 M., Petäjä, T., Worsnop, D. R., Kulmala, M., and Wang, L. J. S.: Atmospheric new particle
626 formation from sulfuric acid and amines in a Chinese megacity, *Science*, 361, 278-281,
627 <https://doi.org/10.1126/science.aao4839>, 2018.
- 628 York, D. M., Darden, T. A., and Pedersen, L. G.: The effect of long-range electrostatic interactions
629 in simulations of macromolecular crystals: A comparison of the Ewald and truncated list
630 methods, *J. Chem. Phys.*, 99, 8345-8348, <https://doi.org/10.1063/1.465608>, 1993.
- 631 Zhang, H., Kupiainen-Määttä, O., Zhang, X., Molinero, V., Zhang, Y., and Li, Z.: The enhancement
632 mechanism of glycolic acid on the formation of atmospheric sulfuric acid-ammonia molecular
633 clusters, *J. Chem. Phys.*, 146, 184308, <https://doi.org/10.1063/1.4982929>, 2017.
- 634 Zhang, H., Wang, W., Pi, S., Liu, L., Li, H., Chen, Y., Zhang, Y., Zhang, X., and Li, Z.: Gas phase
635 transformation from organic acid to organic sulfuric anhydride: Possibility and atmospheric
636 fate in the initial new particle formation, *Chemosphere*, 212, 504-512,
637 <https://doi.org/10.1016/j.chemosphere.2018.08.074>, 2018.
- 638 Zhang, H., Wang, W., Fan, L., Li, J., Ren, Y., Li, H., Gao, R., and Xu, Y.: The role of sulfur cycle in
639 new particle formation: Cycloaddition reaction of SO₃ to H₂S, *J. Environ. Sci.*, 148, 489-501,
640 <https://doi.org/10.1016/j.jes.2023.09.010>, 2025.



- 641 Zhang, J., and Dolg, M.: ABCluster: the artificial bee colony algorithm for cluster global
642 optimization, *Phys. Chem. Chem. Phys.*, 17, 24173-24181,
643 <https://doi.org/10.1039/C5CP04060D>, 2015.
- 644 Zhang, Z., Yin, H., Shang, Y., and Luo, S.-N.: Accurate rate constants for barrierless dissociation of
645 ethanol: VRC-VTST and SS-QRRK calculations with the cheaper DFT method, *Chem. Phys.*
646 *Lett.*, 823, 140522, <https://doi.org/10.1016/j.cplett.2023.140522>, 2023.
- 647 Zhang, Z. P., Wang, S. H., Shang, Y. L., Liu, J. H., and Luo, S. N.: Theoretical study on ethylamine
648 dissociation reactions using VRC-VTST and SS-QRRK methods, *J. Phys. Chem. A*, 128, 2191-
649 2199, <https://doi.org/10.1021/acs.jpca.3c08373>, 2024.
- 650 Zhao, Z., Kong, K., Wang, S., Zhou, Y., Cheng, D., Wang, W., Zeng, X. C., and Li, H. J. T. J. o. P.
651 C. L.: Understanding hygroscopic nucleation of sulfate aerosols: combination of molecular
652 dynamics simulation with classical nucleation theory, *J. Phys. Chem. Lett.*, 10, 1126-1132,
653 <https://doi.org/10.1021/acs.jpcllett.9b00152>, 2019.
- 654 Zhong, J., Zhu, C., Li, L., Richmond, G. L., Francisco, J. S., and Zeng, X. C.: Interaction of SO₂
655 with the surface of a water nanodroplet, *J. Am. Chem. Soc.*, 139, 17168-17174,
656 <https://doi.org/10.1021/jacs.7b09900>, 2017.
- 657 Zhong, J., Li, H., Kumar, M., Liu, J., Liu, L., Zhang, X., Zeng, X. C., and Francisco, J. S.:
658 Mechanistic insight into the reaction of organic acids with SO₃ at the air-water interface, 58,
659 8351-8355, <https://doi.org/10.1002/anie.201900534>, 2019.



660

661

Graphic Abstract



662

Figure Captions

663 **Fig. 1.** Energy diagrams for SO_3 hydrolysis with FSA at the CCSD(T)-F12/cc-pVDZ-F12//M06-
664 2X/6-311++G(2df,2pd) level.

665 **Fig. 2.** BOMD simulations of $\text{HSO}_4 \cdots \text{FSA} \cdots \text{H}_3\text{O}^+$ ion pair formation from SO_3 hydrolysis with
666 FSA at the air-water interface. (Top: Snapshot structures from BOMD simulations, showing the ion
667 pair formation. Bottom: Time evolution of key bond distances S-O1, O5-H3, and O1-H2 during the
668 induced mechanism.)

669 **Fig. 3.** ESP-mapped vdW surfaces of sulfuric acid (SA), ammonia (A) and formic sulfuric anhydride
670 (FSA). Blue, red, yellow, cyan, and white spheres represent N, O, S, C, and H atoms, respectively,
671 with ESP in $\text{kcal}\cdot\text{mol}^{-1}$.

672 **Fig. 4.** (a) Bar graph of aggregation completion time at different atmospheric temperatures; (b)
673 snapshots of nucleation simulation at 258.15 K from FSA, SA and A using the VDW representation,
674 with N_2 and O_2 shown using the line drawing method.

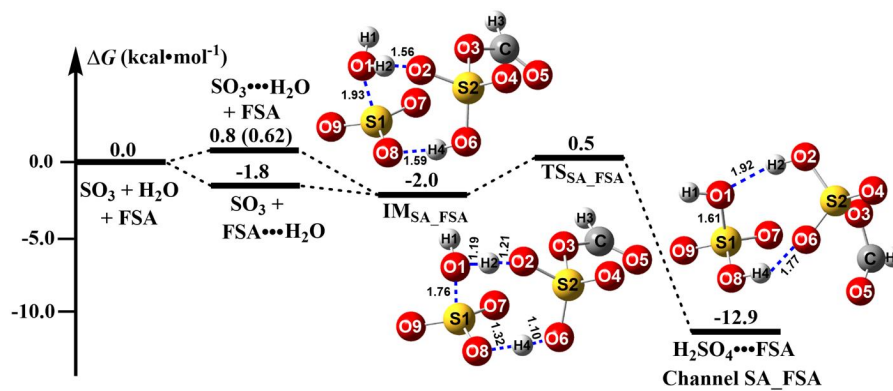
675 **Fig. 5.** Histogram of (a) Gibbs free energy of formation (ΔG , $\text{kcal}\cdot\text{mol}^{-1}$) and (b) evaporation rate
676 coefficient (γ , s^{-1}) for key pure SA-A clusters and FSA-containing stable clusters at 258.15, 278.15
677 and 298.15 K.

678 **Fig. 6.** (a) Cluster formation rate (J , $\text{cm}^{-3}\text{ s}^{-1}$) and (b) enhancement factor R with $[\text{SA}] = 10^6$
679 $\text{molecules}\cdot\text{cm}^{-3}$, $[\text{A}] = 10^9$ $\text{molecules}\cdot\text{cm}^{-3}$ at three temperatures (black: 258.15 K, red: 278.15 K,
680 blue: 298.15 K).

681 **Fig. 7.** (a) The cluster formation rate (J , $\text{cm}^{-3}\text{ s}^{-1}$) and (b) enhancement factor R as a function of $[\text{A}]$
682 with $[\text{FSA}] = 10^6$ $\text{molecules}\cdot\text{cm}^{-3}$ at 278.15 K for five $[\text{SA}]$ levels (black: 10^4 , red: 10^5 , blue: 10^6 ,
683 green: 10^7 , purple: 10^8 $\text{molecules}\cdot\text{cm}^{-3}$).

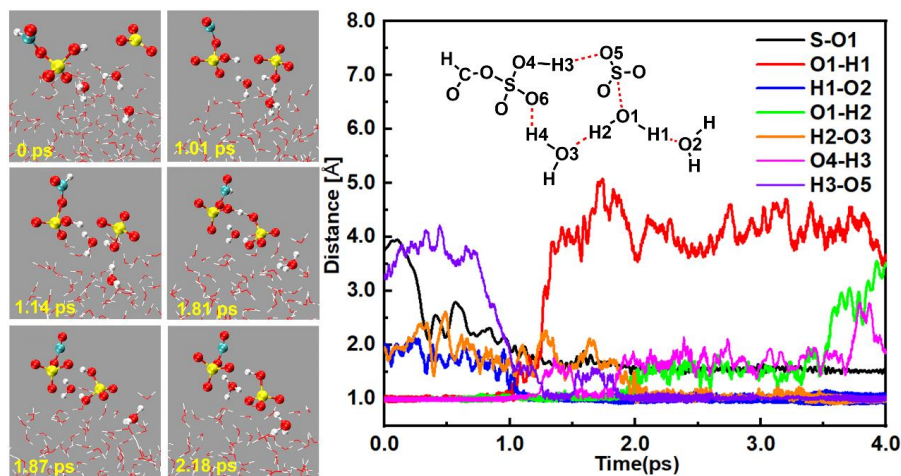
684 **Fig. 8.** Primary growth pathways of clusters at $T = 278.15$ K, $[\text{SA}] = 10^6$ $\text{molecules}\cdot\text{cm}^{-3}$, $[\text{A}] = 10^9$
685 $\text{molecules}\cdot\text{cm}^{-3}$, and $[\text{FSA}] = 10^3$ - 10^7 $\text{molecules}\cdot\text{cm}^{-3}$. Blue and orange arrows represent the SA-A-
686 based and SA-A-FSA-based pathways, respectively.

687 **Fig. 9.** Influence of (a) temperature, (b) $[\text{SA}]$, (c) $[\text{A}]$ and (d) $[\text{FSA}]$ on the relative contribution of
688 the pure SA-A pathway and the FSA-containing pathway to the flux out of the system.



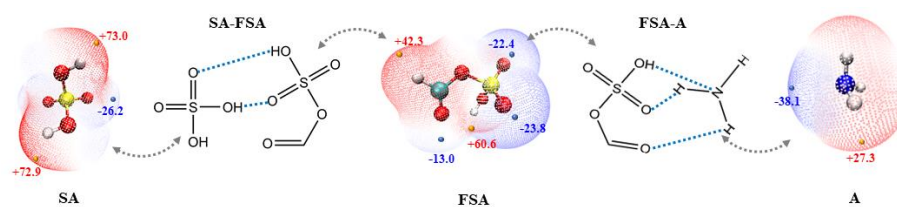
689

690 **Fig. 1.** Energy diagrams for SO₃ hydrolysis with FSA at the CCSD(T)-F12/cc-pVDZ-F12//M06-
691 2X/6-311++G(2df,2pd) level.



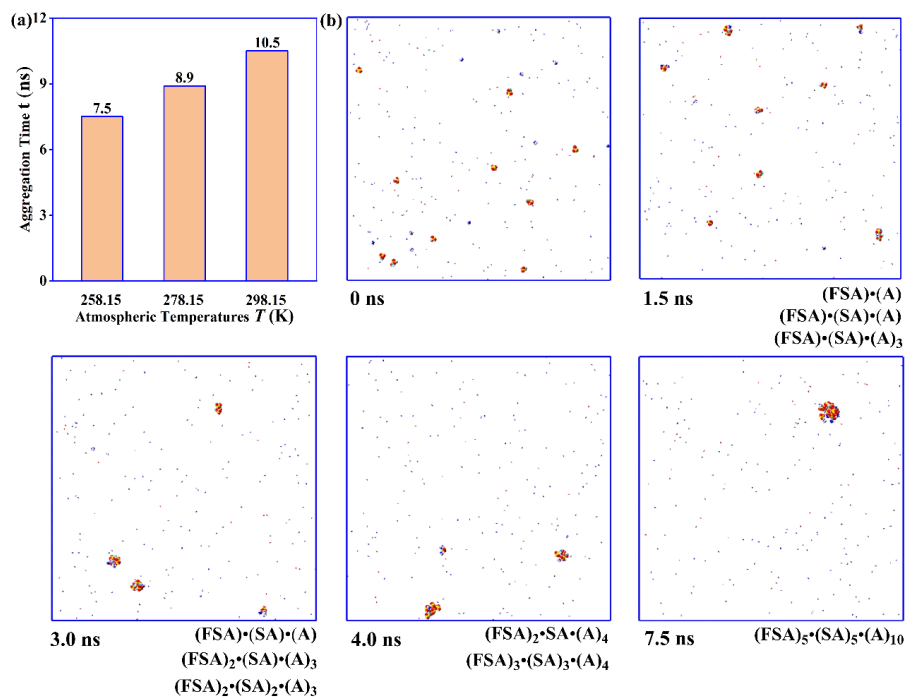


697

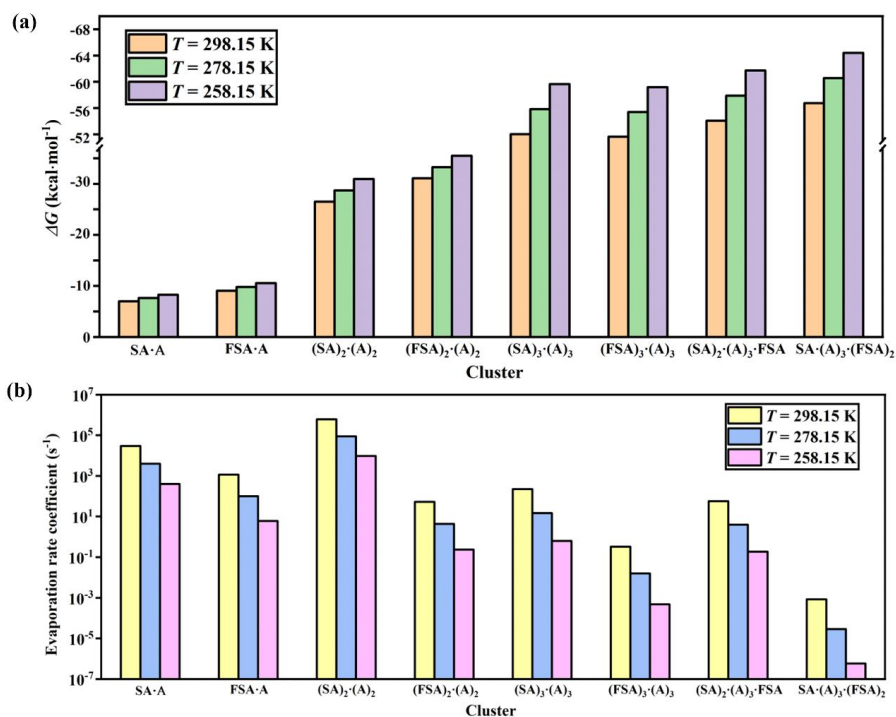


698

699 **Fig. 3.** ESP-mapped vdW surfaces of sulfuric acid (SA), ammonia (A) and formic sulfuric anhydride
700 (FSA). Blue, red, yellow, cyan, and white spheres represent N, O, S, C, and H atoms, respectively,
701 with ESP in kcal·mol⁻¹.

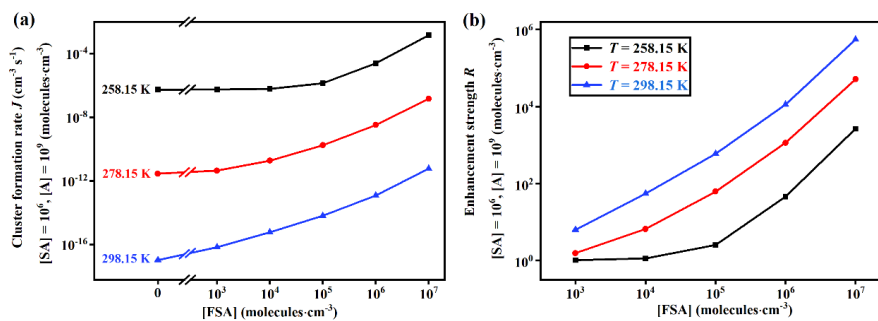


702
 703 **Fig. 4.** (a) Bar graph of aggregation completion time at different atmospheric temperatures; (b)
 704 snapshots of nucleation simulation at 258.15 K from FSA, SA and A using the VDW representation,
 705 with N_2 and O_2 shown using the line drawing method.



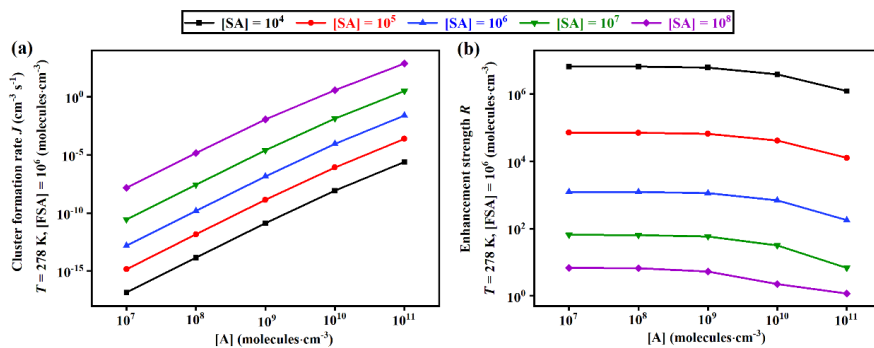
706

707 **Fig. 5.** Histogram of (a) Gibbs free energy of formation (ΔG , kcal·mol⁻¹) and (b) evaporation rate
708 coefficient (γ , s⁻¹) for key pure SA-A clusters and FSA-containing stable clusters at 258.15, 278.15
709 and 298.15 K.



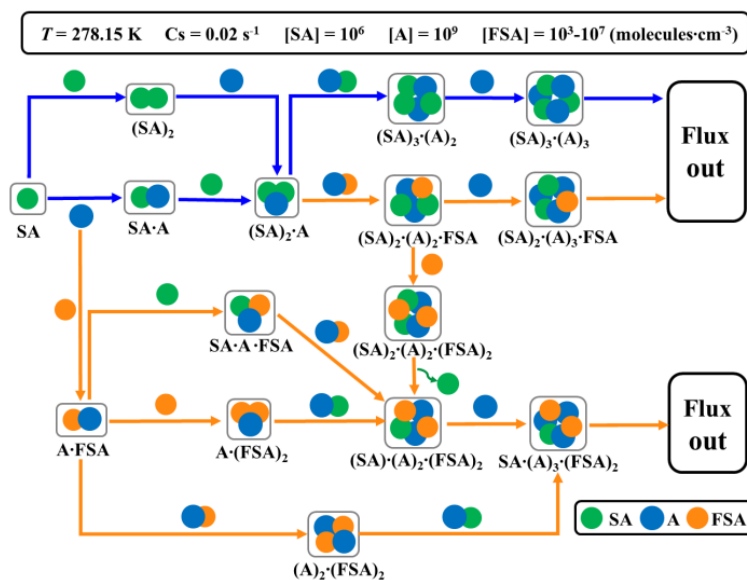
710

711 **Fig. 6.** (a) Cluster formation rate (J , $\text{cm}^3 \text{s}^{-1}$) and (b) enhancement factor R with $[\text{SA}] = 10^6$
712 $\text{molecules} \cdot \text{cm}^{-3}$, $[\text{A}] = 10^9$ $\text{molecules} \cdot \text{cm}^{-3}$ at three temperatures (black: 258.15 K, red: 278.15 K,
713 blue: 298.15 K).

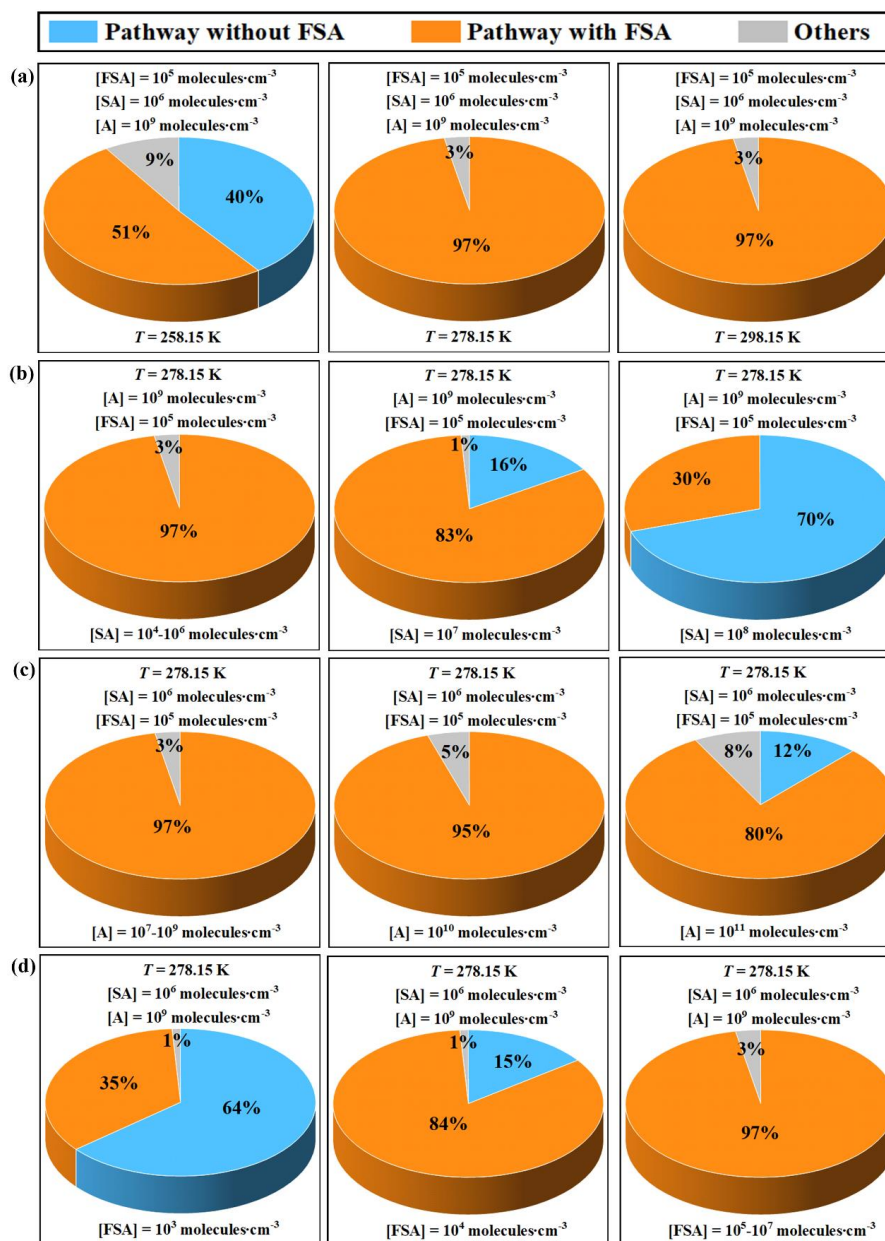


714

715 **Fig. 7.** (a) The cluster formation rate (J , $\text{cm}^{-3} \text{s}^{-1}$) and (b) enhancement factor R as a function of $[A]$
716 with $[FSA] = 10^6 \text{ molecules} \cdot \text{cm}^{-3}$ at 278.15 K for five $[SA]$ levels (black: 10^4 , red: 10^5 , blue: 10^6 ,
717 green: 10^7 , purple: $10^8 \text{ molecules} \cdot \text{cm}^{-3}$).



718
 719 **Fig. 8.** Primary growth pathways of clusters at $T = 278.15 \text{ K}$, $[SA] = 10^6 \text{ molecules}\cdot\text{cm}^{-3}$, $[A] = 10^9$
 720 $\text{molecules}\cdot\text{cm}^{-3}$, and $[FSA] = 10^3\text{-}10^7 \text{ molecules}\cdot\text{cm}^{-3}$. Blue and orange arrows represent the SA-A-
 721 based and SA-A-FSA-based pathways, respectively.
 722



723
 724 **Fig. 9.** Influence of (a) temperature, (b) [SA], (c) [A] and (d) [FSA] on the relative contribution of
 725 the pure SA-A pathway and the FSA-containing pathway to the flux out of the system.



726 **Table 1.** Rate constants ($\text{cm}^3 \cdot \text{molecule}^{-1} \cdot \text{s}^{-1}$) for SO_3 hydrolysis with and without FSA, H_2O , and X
727 ($X = \text{HNO}_3, \text{HCOOH}, (\text{COOH})_2$ and H_2SO_4) within the temperature range of 280-320 K

T/K	$k_{\text{SA_FSA}}$	k_{SA}	$k_{\text{SA_WM}}$	$k_{\text{SA_FA}}$	$k_{\text{SA_NA}}$	$k_{\text{SA_OA}}$	$k_{\text{SA_SA}}$
280	7.94×10^{-11}	6.24×10^{-24}	1.68×10^{-12}	8.88×10^{-11}	1.26×10^{-12}	8.02×10^{-11}	5.60×10^{-11}
290	7.84×10^{-11}	8.12×10^{-24}	1.45×10^{-12}	8.17×10^{-11}	1.05×10^{-12}	7.74×10^{-11}	5.08×10^{-11}
298	7.71×10^{-11}	1.02×10^{-23}	1.28×10^{-12}	7.60×10^{-11}	9.11×10^{-13}	7.48×10^{-11}	4.69×10^{-11}
300	7.67×10^{-11}	1.09×10^{-23}	1.24×10^{-12}	7.46×10^{-11}	8.80×10^{-13}	7.42×10^{-11}	4.59×10^{-11}
310	7.46×10^{-11}	1.50×10^{-23}	1.07×10^{-12}	6.78×10^{-11}	7.46×10^{-13}	7.06×10^{-11}	4.13×10^{-11}
320	7.21×10^{-11}	2.12×10^{-23}	9.22×10^{-13}	6.12×10^{-11}	6.46×10^{-13}	6.68×10^{-11}	3.70×10^{-11}

728



729 **Table 2.** Binding free energy ($\text{kcal}\cdot\text{mol}^{-1}$) for the formation of various clusters at 298 K.

FSA ⁻ -SA	FSA ⁻ -HNO ₃	H ₃ O ⁺ -A	H ₃ O ⁺ -SA	SA-A
-21.2	-12.1	-51.7 (-49.2) ^a	-27.5 (-27.0) ^a	-8.9 (-8.9) ^a
HSO ₄ ⁻ -SA	HSO ₄ ⁻ -(COOH) ₂	HSO ₄ ⁻ -HNO ₃	SA-A-FSA ⁻	SA-A- HOOCCH ₂ COOH
-41.6	-33.6	-27.8	-25.6	-13.1(13.6) ^b
SA-A- HOCCOOSO ₃ H	SA-A- CH ₃ OSO ₃ H	SA-A- HOCH ₂ COOH	SA-A-HOOCCH ₂ CH(NH ₂)COOH	
-20.4 (-22.5) ^c	-18.8 (-20.7) ^d	-13.2 (-14.0) ^e	-12.8 (-13.5) ^f	

730 Energies are given in $\text{kcal}\cdot\text{mol}^{-1}$ and calculated at the M06-2X/6-311++G(2df,2pd) level of theory. References are as
731 follows: ^a Zhong et al. (2019), ^b Zhang et al. (2018), ^c Rong et al. (2020), ^d Gao et al. (2023), ^e J. Liu et al. (2021), ^f
732 Zhang et al. (2017).